Article ID: 1000-324X(2019)04-0444-11 **DOI:** 10.15541/jim20180466

Zirconia Incorporation in 3D Printed β-Ca_2SiO_4 Scaffolds on Their Physicochemical and Biological Property

FU Sheng-Yang[1], YU Bin[2], DING Hui-Feng[2,3], SHI Guo-Dong[2], ZHU Yu-Fang[1]

(1. School of Materials Science and Engineering, University of Shanghai for Science and Technology, Shanghai 200093, China; 2. Department of Orthopedics, Shanghai Public Health Clinical Center, Shanghai Medical School, Fudan University, Shanghai 200032, China; 3. Department of Orthopedics, Shanghai Pudong Hospital, Fudan University Pudong Medical Center, Shanghai 201399, China)

Abstract: 3D printed bioceramics derived from preceramic polymers are of great interest in bone tissue engineering due to their simplified fabrication processes. In this study, three-dimensional (3D) porous β-Ca_2SiO_4 scaffolds incorporated with ZrO_2 were fabricated from silicone resin loaded with active $CaCO_3$ and inert ZrO_2 fillers by 3D printing. The fabricated scaffolds possessed uniform interconnected macropores with a high porosity (> 67%). The results showed that the increase of ZrO_2 incorporation significantly enhanced the compressive strength, and stimulated cell proliferation and differentiation of osteoblasts. Importantly, the *in vivo* results indicated that the ZrO_2-incorporated β-Ca_2SiO_4 scaffolds improved osteogenic capacity compared to pure β-Ca_2SiO_4 scaffolds. Taken together, the ZrO_2-incorporated β-Ca_2SiO_4 scaffolds fabricated by combining polymer-derived strategy with 3D printing could be a promising candidate for bone tissue engineering.

Key words: β-Ca_2SiO_4; ZrO_2; polymer-derived; 3D printing; bone tissue engineering

A wide range of silicate-based bioceramics have attracted great attention in the past two decades due to their excellent bioactivity for bone tissue engineering[1-5]. Silicate-based bioceramics are able to degrade after implanted in bone defects. Meanwhile, the formation of bone-like hydroxyapatite layers on the surface of bioceramics induces a strong chemical-force bonding to tissue. β-Ca_2SiO_4 ceramic is one of silicate-based bioceramics with excellent bioactivity, and also has the ability to support osteogenic-related cells and enhance new bone formation[6-9].

It has been accepted that porous scaffold structure is vital for bone tissue engineering. An ideal scaffold with interconnected macroporous structure promotes cells migration, nutrients transfer, vascularization and bone regeneration[10]. For example, Dai, *et al*[6] proposed a polyurethane foam templating method to prepare porous β-Ca_2SiO_4 ceramic scaffolds using $CaCO_3$ and SiO_2 powders. A mixture of $CaCO_3$ and SiO_2 powders were added into polyurethane foam with different weight ratio, and porous β-Ca_2SiO_4 with a regulated porosity (54.2%–83.4%) could be formed after heat treatment[6]. Other methods including porogen templating, gel-cast foaming and freeze drying have also been used to fabricate porous β-Ca_2SiO_4 bioceramics[11-13]. However, such methods are not precise enough to control pore shape, size and interconnectivity[14].

3D printing technique is able to control the architectures of scaffolds, including external morphology and internal pore structure at a micron level[10,15-19]. In the past few years, a variety of silicate-based bioceramics have been fabricated by 3D printing, such as bioactive glass[15-16,20-23], hydroxyapatite[24], calcium phosphate and calcium silicate[14,25]. In general, the fabrication of 3D printed bioceramic scaffolds involves in three steps: preparation of ceramic powders, 3D printing with polymer binders, and sintering for densification. Nevertheless, fabrication of silicate-based bioceramic scaffolds by 3D printing is still challenging.

Polymer-derived strategy has shown great potential in fabricating bioceramics in past few years. Due to the outstanding shapeable ability of preceramic polymers, it

Received date: 2018-10-06; **Modified date:** 2018-10-28

Foundation item: National Natural Science Foundation of China (51872185); The Science and Technology Commission of Shanghai Municipality (17060502400); The State Key Laboratory for Modification of Chemical Fibers and Polymer Materials, Donghua University (LK1616); Academic Leaders Training Program of Pudong Health Bureau of Shanghai (PWRd2017-03); Science and Technology Development Fund of Shanghai Pudong New Area (PKJ2015-Y37); "Pu Jing" Training Program of Shanghai Pudong hospital (PJ201503)

Biography: FU Sheng-Yang (1994–), male, candidate for Master degree. E-mail: fushengyang@sina.com; YU Bin (1988–), male, candidate for PhD degree. E-mail: binyu13@126.com

Corresponding authors: DING Hui-Feng, professor. E-mail: dinghf0118@163.com; ZHU Yu-Fang, professor. E-mail: zjf2412@163.com

is easy to shape bioceramics into complex morphology with controllable pore structures. Thus, the combination of polymer-derived strategy with 3D printing technique can be promising for the fabrication of scaffolds. Recently, Bernando, *et al*[26-31] proposed to fabricate silicate-based bioceramic scaffolds by combining 3D printing with polymer-derived technique. As a silicon source, silicone resin is easily shaped by 3D printing, loaded with active fillers such as $CaCO_3$, $Mg(OH)_2$. Next, the active fillers react with the decomposition products of silicone resin to form silicate-based bioceramics due to the solid reaction during heat treatment. Zocca, *et al*[28] successfully fabricated wollastonite-based bioceramic scaffolds by 3D printing. Silicone resin was dissolved in organic solvents and loaded with $CaCO_3$ powders in a quantitative ratio, and the wollastonite scaffolds formed after 3D printing and sintering at 900 ℃. Furthermore, the incorporation of bioactive glass AP40 in the wollastonite scaffolds improved the biological properties. Similarly, Elsayed, *et al*[27] fabricated wollastonite-diopside scaffolds by direct ink writing of silicone resin, $CaCO_3$ and $Mg(OH)_2$, which showed high compressive strength (3.9–4.9 MPa) with a porosity of 68%–76%.

Our group successfully fabricated porous β-Ca_2SiO_4 scaffolds derived from preceramic resin loaded with $CaCO_3$ active filler by 3D printing recently[32]. The fabricated β-Ca_2SiO_4 scaffolds had uniform interconnected macropores, high porosity and excellent apatite mineralization ability. Howbeit, the mechanical strength of the scaffolds should be enhanced although it meets the requirement of human trabecular bone (2–12 MPa), and high dissolution rate of the scaffolds might result in an alkali microenvironment, which is detrimental to the cells[33]. As we know, zirconia (ZrO_2) has been successfully used in clinic due to the toughest property in oxide ceramics[34-36], and the excellent biocompatibility endows the ZrO_2 scaffolds with bone tissue engineering. ZrO_2 is inert *in vitro* or *in vivo*, which shows great chemical stability and the ability to enhance mechanical strength. Although ZrO_2 is not degradable, small dose of ZrO_2 has little side effect, according to the commercial ZrO_2 use in dental implants. Therefore, the introduction of ZrO_2 into pure ceramics may probably regulate the degradation rate, and create a more stable microenvironment for related cell activities, and eventually promoting new bone formation.

In this study, we proposed to fabricate the ZrO_2-incorporated porous β-Ca_2SiO_4 ceramic scaffolds by polymer-derived technique and 3D printing, and aimed to enhance the mechanical strength, chemical stability and biological properties of β-Ca_2SiO_4 scaffolds. As shown in Scheme 1, a printing paste was prepared by mixing silicone resin, active $CaCO_3$ and passive ZrO_2 fillers. The ZrO_2-incorporated porous β-Ca_2SiO_4 ceramic scaffolds were obtained after 3D printing and sintering. Furthermore, the effect of the ZrO_2 incorporation in β-Ca_2SiO_4 scaffolds on physicochemical and biological properties were systemically investigated.

1 Materials and methods

1.1 Materials

A commercial silicone resin (polysilsesquioxane, Silres®MK) was purchased from WackerChemie (Munich, Germany). Calcium carbonate ($CaCO_3$, ≥99.0%), zirconia (ZrO_2, ≥99.0%) and isopropyl alcohol (IPA, ≥99.7%) were purchased from Sinopharm Chemical Reagent Co. Ltd (Shanghai, China).

1.2 3D printing of $CaCO_3$/ZrO_2/silicone green scaffolds and ceramization

In this study, the 4th 3D Bioplotter™ (EnvisionTEC GmbH, Germany) was used to print $CaCO_3$/ZrO_2/silicone green scaffolds. Firstly, $CaCO_3$ and ZrO_2 powders were sieved through 37 μm sieves to obtain uniform powders with the particle size less than 38 μm. Here, $CaCO_3$ powder was substituted by ZrO_2 powder with different ratio (0, 5mol%, 10mol%, and 15mol%). Subsequently, 1.0 g silicone resin was dissolved into 0.7 mL isopropyl alcohol absolutely, and then the sieved $CaCO_3$/ZrO_2 powders were added into silicone solution (W_{CaCO_3/ZrO_2} : $W_{silicone}$ = 2.8 : 1). The mixture was stirred at room temperature to form an injectable paste. Finally, the prepared injectable paste was moved into a plastic cartridge, which was fixed on the printing device.

Simultaneously, cylinder models (diameter=10 mm, height=10 mm) was loaded on the Bioplotter CAD/CAM software. Through the extrusion of the paste as a fiber, the scaffolds were plotted with layer-by-layer, up to 31 layers, and the angle of successive layers was about 60°. The dosing pressure of syringe pump was 2.0–4.0 bar and the moving speed of the working syringe was 4.0–5.0 mm/s, the nozzle size was 400 μm. After drying in 37 ℃ oven for 24 h, the green scaffolds were sintered

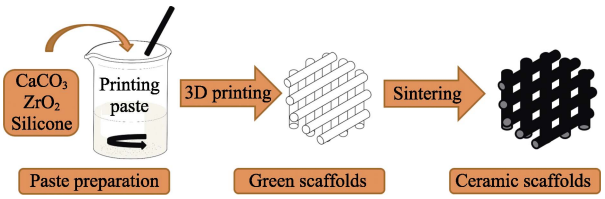

Scheme. 1　Fabrication process of the ZrO_2-incorporated β-Ca_2SiO_4 scaffolds

at different temperatures (1000, 1100, 1200 ℃) for 3 h with a 2 ℃/min heating rate in argon atmosphere. The final scaffolds were named as 0Zr-C2S, 5Zr-C2S, 10Zr-C2S and 15Zr-C2S for those scaffolds incorporated with 0 ZrO_2, 5mol% ZrO_2, 10mol% ZrO_2 and 15mol% ZrO_2.

1.3 Characterizations

A wide-angle XRD patterns were obtained on a Bruker D8 advance X-ray powder diffractometer using CuKα1 radiation 0.15405 nm (Bruker Corp., Billerica, MA, USA). FT-IR spectra were recorded on a LAM750(s) spectrometer in transmission mode. After the scaffolds were coated with gold using a sputter coater (Desk-II, Denton Vacuum Inc), scanning electron microscopy (SEM) was carried out with a FEI Quanta 450 field emission scanning electron microscope. The compressive strength of the scaffolds was tested using a static materials testing machine (2.5 kN) (Zwick Roell, Ulm, Germany) at a crosshead speed of 0.5 mm/min. The porosity of the scaffolds was measured by using Archimedes' principle and water was used as liquid medium. The porosity (P) was calculated according to the following formulation: $P=(W_{sat}-W_{dry})/(W_{sat}-W_{sus})\times100\%$, where W_{dry} is the dry weight of the scaffolds, W_{sus} is the weight of the scaffolds suspended in water, W_{sat} is the weight of the scaffolds saturated with water.

1.4 The degradation and apatite formation ability of scaffolds

All the sintered scaffolds were incubated into a fresh-made simulated body fluid (SBF) at a ratio of 200 mL SBF per gram scaffold at 37 ℃. The pH value of SBF was measured every day for 7 and the residual weight of the scaffolds was weighed over a period of 28 d with changing SBF after each time measurement. Scanning electron microscopy (SEM) with energy dispersive spectrometry (EDS) and FT-IR were used to observe the surface morphology and composition of all testing scaffolds after soaking in SBF for 7 d.

1.5 Cell culture and seeding

The rat bone marrow mesenchymal cells (rBMSC) were derived from tibias and femurs of 4-week-old male Sprague−Dawley (SD) rats. Rats were sacrificed under the approval of the Institutional Animal Care and Use Committee at our institution. Animals were sterilized by immersion in 75% alcohol before dissection. Tibias and femurs were dissected aseptically and carefully removed all connective tissues, then washed with cold PBS thrice. Bone marrow were harvested by flushing each long bone with cold PBS and filtered through a 70 μm nylon mesh to remove debris and collected into new tubes. After centrifuging at 1000 g for 5 min at RT, cells were suspended in the culture medium in α-MEM medium (Hyclone, USA) with 10% fetal bovine serum (FBS, Gibco, USA), 100 U/mL penicillin-streptomycin (Sigma) and left onto plates in the humidified incubator at 37 ℃ with 5% CO_2. On day 3, non-adherent cells were removed by change of medium. The third passage of rBMSCs were utilized for the following cell proliferation and differentiation on scaffolds *in vitro*. Cells were cultured in α-MEM medium (Hyclone, USA) with 10% fetal bovine serum (FBS, Gibco, USA), 100 U/mL penicillin-streptomycin (Sigma) in a humidified incubator at 37 ℃ with 5% CO_2, and the medium was replaced every two days for a period up to 7 d. All scaffolds were sterilized with ethylene oxide, followed by immersing in the medium at least 24 h. Then, scaffolds were transferred into a non-treated 24-well or six-well plate and cells in the logarithmic phase at the density of 1×10^4 cells/well, 2×10^4 cells/well respectively were seeded.

1.6 Cell proliferation and ALP activity

Cells with an initial density of 1×10^4 per scaffold per well were seeded in 24-well plate. Cell proliferation on the scaffolds was evaluated by Cell Counting kit-8 assay (CCK-8, Dojindo, Japan) after the cells had been seeded and cultured for 1, 3 and 7 d. For CCK-8 test, the medium was removed and 360 μL of new medium and 40 μL of CCK-8 solution was added to each well. The cells were then incubated at 37 ℃ in a humidified atmosphere containing 5% CO_2 for 2 h. Optical density (OD) values were evaluated at 450 nm through a microplate reader (TECAN Infinite 200 pro, Switzerland). The relative cell viability was defined as the mean percentage of viable cells compared to the control cells.

ALP activity was assayed using an ALP assay kit (Cat. No. P0321, Beyotime). 1×10^5 cells were seeded on each scaffold in a 24-well plate and cultured for 7 and 14 d. At each time point, cells were washed gently three times with PBS and followed by washing once in cold 50 mmol/L Tris buffer, and then cells were lysed in 200 mL of 0.2% Triton X-100. Lysates were centrifuged at 14000 r/min for 15 min at 4 ℃, and added 50 mL supernatant into 150 mL working solution according to the manufacturer's protocol (Beyotime). The absorbance was determined at 405 nm with a microplate reader (TECAN Infinite 200 pro, Switzerland). To calculate the ALP activity, a standard curve was needed after normalizing to the total protein content by a MicroBCA protein assay kit (Pierce) at 570 nm with a microplate reader (TECAN Infinite 200 pro, Switzerland). The results were expressed in μmol/L of *p*-nitrophenol released per min per mg of protein.

1.7 Real-time polymerase chain reaction (RT-PCR)

The transcription expression levels of osteoblast differentiation related genes such as collagen type I (COL1), osteocalcin (OCN), runt-related transcription factor 2 (Runx2) and osteopontin (OPN), were measured using quantitative reverse transcription polymerase chain reaction (qRT-PCR) analysis. Briefly, cells were seeded in six-well plate at a density of 1×10^5 cells per scaffold and harvested using TRIzol Reagent (Invitrogen Pty Ltd, Australia) to extract the total messenger ribonucleic acid (mRNA) 7 days, 14 days later respectively. The obtained mRNA was reverse-transcribed into complementary DNA (cDNA) using RevertAid First Strand cDNA Synthesis Kit (Thermo) and then performed qRT-PCR analysis on an ABI Prism 7300 Thermal Cycler (Applied Biosystems, Australia) using SYBR Green detection reagent. The relative expression of the genes mentioned above was normalized against the housekeeping gene glyceraldehyde 3-phosphate dehydrogenase (GAPDH). All samples were assayed in triplicate, and experiments were performed independently. The mean cycle threshold (C_t) value of each target gene was normalized against the C_t value of GAPDH. The relative expression was calculated using the following formula: $2^{-(\text{normalized average } C_t)}\times 100$.

1.8 Surgical procedure, Micro-CT and histological observation

All animal experimental procedures were approved by the Animal Research Committee of Shanghai Pudong Hospital affiliated to Fudan University. 12-week-old male Sprague-Dawley rats were used for surgical procedures. A 1.5 cm sagittal incision was made on the scalp, and the calvarium was exposed by blunt dissection. Two critical-sized defects were created in each rat by means of a 5 mm diameter electric trephine. The 0Zr-C2S and 15Zr-C2S scaffolds (5 mm in diameter and 6 mm in thickness) were respectively embedded in the left and right defect of 9 rats. Three rats were set for blank control. The incision was closed in layers using resorbable sutures. Each animal received an intramuscular injection of penicillin post-operation.

After harvesting the skulls at 8 weeks post-operatively, micro-CT (Skyscan 1176, Kontich, Belgium) was used to evaluate new bone formation. And each undecalcified samples scanned at 18 μm resolution. 3-D images were reconstructed using the 3-D Creator software. Bone volume to total bone volume (BV/TV), local bone mineral densities (BMDs) were also determined using the analysis software.

Samples were decalcified using 5% nitric acid for 1 week with solution replacement every 2 days. Samples were dehydrated with graded EtOH (70%−100%), toluene, and paraffin. Dehydrated samples were embedded in paraffin wax and hardened into a paraffin block for sectioning. Specimens were cut to 5 μm using a microtome (HM325, Thermo scientific). Sections underwent deparaffinization and hydration and stained nuclei and cytosol with Masson stain to identify new bone formation. Blue indicated new bone formation, and the scaffolds showed black. The photos were obtained by histology digital scanning system (ScanScope CS2, Leica Biosystems). The surface areas of the newly formed bone and material residue were measured using Image Pro Plus™ (Media Cybernetics, Silver Springs, MD) based on the entire bone defect area.

1.9 Statistical analysis

Three separate experiments were carried out to collect the data. Then, the data was expressed as means ± standard deviation. The level of significance was determined by the one-way ANOVA and Student-Newman-Keuls post hoc tests, and P values < 0.05 were considered to be significant.

2 Results

2.1 Fabrication and characterization of the scaffolds

The phases of 3D printed scaffolds incorporated with different ZrO_2 contents and sintered at different temperatures were examined by XRD. As shown in Fig. 1(A), similar diffraction peaks are appeared for the scaffolds with different ZrO_2 content, and these peaks are assigned to ZrO_2 (monoclinic and tetragonal refers to JCPDS card 37-1484 and 42-1164, respectively) and β-Ca_2SiO_4 phase (JCPDS card 33-0302). The intensity of diffraction peaks for ZrO_2 phase becomes higher with the increase of ZrO_2 content. On the other hand, XRD patterns of the ZrO_2-incorporated β-Ca_2SiO_4 scaffolds sintered at different temperature are shown in Fig. 1(B). It can be clearly seen that most of ZrO_2 is tetragonal structure in the scaffolds sintered at 1200 ℃, while monoclinic ZrO_2 structure dominates in the scaffolds sintered at 1000 and 1100 ℃. As shown in FT-IR spectra of the scaffolds (Fig. 1(C)), the bands at 992 and 845 cm^{-1} were assigned to the Si–O–Si and Si–O stretching vibration respectively, and the band at 519 cm^{-1} was assigned to the Si–O–Si bending vibration, which indicated the formation of silicate as well.

Fig. 2 shows the surface and fracture morphologies of the scaffolds incorporated with different ZrO_2 content sintered at 1200 ℃ for 3 h. Each type of the ZrO_2-incorporated β-Ca_2SiO_4 scaffolds had parallel struts and regular porous structure with a macropore size of ca.

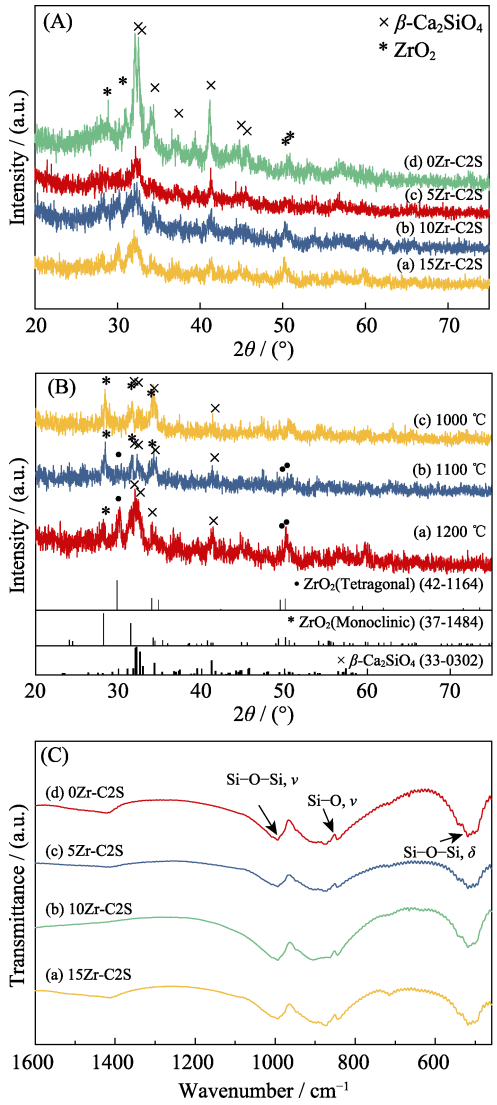

Fig. 1 (A) XRD patterns of the scaffolds incorporated with different ZrO_2 content sintered at 1200 ℃, (B) 15Zr-C2S scaffolds sintered at different temperature, and (C) FT-IR spectra of the β-Ca_2SiO_4 scaffolds incorporated with different ZrO_2 content sintered at 1200 ℃.

400 μm. The rough surfaces and micron-scale pores on the struts of scaffolds were easily observed. With the increase of ZrO_2 content in the scaffolds, the densification degree was not significantly different. The weight content of ZrO_2 in the scaffolds estimated by the EDS analysis were 0, 0.91wt%, 1.31wt% and 4.10wt% for 0Zr-C2S, 5Zr-C2S, 10Zr-C2S, and 15Zr-C2S scaffolds respectively. The fracture behavior of all scaffolds were brittle fracture, while the rough morphologies and micro-scale pores were also observed in the fracture sections. On the other hand, the crystal size of pure β-Ca_2SiO_4 scaffolds were in micro level, and its crystallinity was much higher compared to the ZrO_2-incorporated β-Ca_2SiO_4 scaffolds, which was consistent with the XRD results.

Fig. 3 shows the compressive strength and porosity of the ZrO_2-incorporated β-Ca_2SiO_4 scaffolds. With the increase of ZrO_2 content in the scaffolds, the compressive strength enhanced and which are estimated to be (3.9±0.8) MPa, (4.7±0.4) MPa, (5.4±0.1) MPa and (6.1±0.4) MPa for the 0Zr-C2S, 5Zr-C2S, 10Zr-C2S, and 15Zr-C2S scaffolds respectively. On the other hand, the porosity of the ZrO_2-incorporated β-Ca_2SiO_4 scaffolds are about (71.0±0.1)%, (73.1±1.4)%, (71.0±1.8)% and (67.5±1.3)% with no significant difference.

2.2 Degradation and apatite mineralization ability of the scaffolds

The variation of pH value in micro-environment and the residual weight of each type of ZrO_2-incorporated β-Ca_2SiO_4 scaffolds immersed in SBF are shown in Fig. 4(A–B). It can be observed that pH increased with soaking time, and became more stable with the increase of the ZrO_2 incorporation. After soaking in SBF for 7 days, pH values for each type of ZrO_2-incorporated β-Ca_2SiO_4 scaffolds were 8.46±0.08, 8.43±0.04, 8.30± 0.03 and 8.27±0.08, respectively. In addition, the degradation of each type of ZrO_2-incorporated β-Ca_2SiO_4 scaffolds were observed obviously. The weight loss of all scaffolds increased with soaking time, which also exhibited more stable with the increase of the ZrO_2 incorporation. The residual weight of each type of ZrO_2-incorporated β-Ca_2SiO_4 scaffolds were about (48.37±3.50)%, (55.74±3.74)%, (56.21±3.36)% and (59.43± 3.57)%, respectively.

The apatite forming ability was evaluated by FT-IR and SEM in Fig. 4 (C-D). As shown in SEM images, all of scaffolds kept the interconnected pore structure, a thick layer composed of the spherical particles formed on the surface. FT-IR spectra of the SBF-soaked scaffolds showed the bands at 1063-1093 cm^{-1}, which were assigned to stretching vibration of P–O, and the bands at 873 and 1424 cm^{-1} were attributed to stretching vibration of C–O. These results indicated the formation of apatite on the scaffolds. Moreover, some newly formed pores on each strut could be observed.

2.3 Cell responses to the scaffolds

rBMSCs were used in this study to investigate cell responses to the ZrO_2-incorporated β-Ca_2SiO_4 scaffolds. Fig. 5 shows the attachment of rBMSCs on the ZrO_2-incorporated β-Ca_2SiO_4 scaffolds. It could be observed that rBMSCs were able to attach on the struts of all scaffolds, and the spreading state seemed no difference, suggesting all of scaffolds were biocompatible to rBMSCs.

Fig. 6 shows the cell proliferation and ALP activity of rBMSCs on the ZrO_2-incorporated scaffolds. The results revealed that the ZrO_2-incorporated scaffolds supported cell proliferation. The ability of cell proliferation increased over time, and improved with the increase of ZrO_2 incorporation. Moreover, the proliferation on the

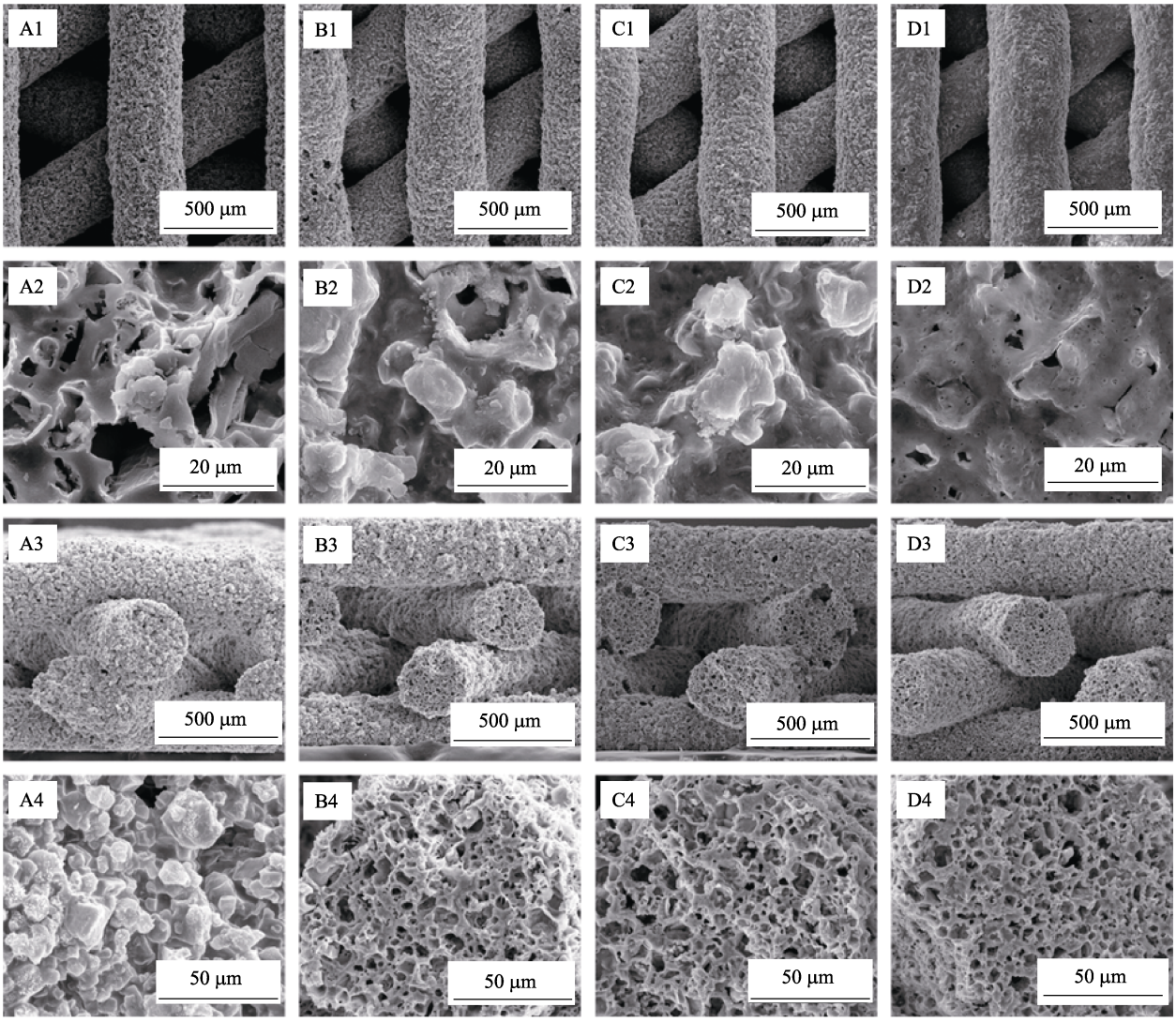

Fig. 2　SEM images of (A) 0Zr-C2S, (B) 5Zr-C2S, (C) 10Zr-C2S and (D) 15Zr-C2S scaffolds, with SEM fracture surface images from (A3-A4) to (D3-D4)

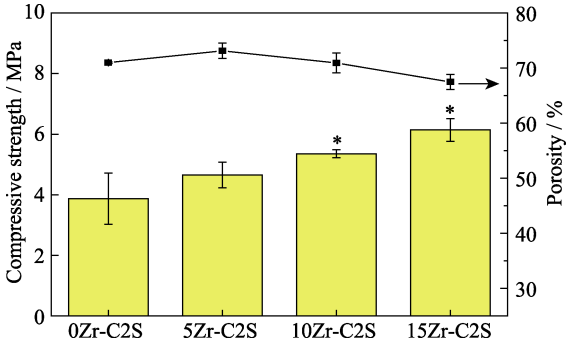

Fig. 3　The compressive strength and porosity of the ZrO_2-incorporated β-Ca_2SiO_4 scaffolds (n = 3; * indicated significant differences, $P < 0.05$)

ZrO_2-incorporated β-Ca_2SiO_4 scaffolds was a little higher than that on pure β-Ca_2SiO_4 scaffolds for 7 d. ALP activities of rBMSCs cultured on scaffolds for 7, 14 d are shown in Fig. 6(B), which indicate the differentiation ability of osteoblasts. Similar to the results of cell proliferation, ALP activities improved over time and the ALP activities on the ZrO_2-incorporated β-Ca_2SiO_4 scaffolds was a little higher compared to that on pure β-Ca_2SiO_4 scaffolds.

Cell differentiation of rBMSCs on the ZrO_2-incorporated β-Ca_2SiO_4 scaffolds was further evaluated by related osteogenic expression, determined by the expression of osteogenic markers at 7 and 14 days (Fig. 7). The expression of the COL-1, OCN, Runx-2 and OPN genes cultured on all of scaffolds was upregulated over time, and the expression level improved when ZrO_2 was incorporated in the scaffolds, and 15Zr-C2S scaffolds showed the highest osteoblast related-gene expression.

2.4　Analysis of bone regeneration in calvarial defects

The morphology of the newly formed bone in defect sites was reconstructed by micro-CT, and the quantity was estimated by morphometrical analysis. The results showed that the newly formed bone area in the 0Zr-C2S and 15Zr-C2S scaffolds was greater after 8 weeks implantation.

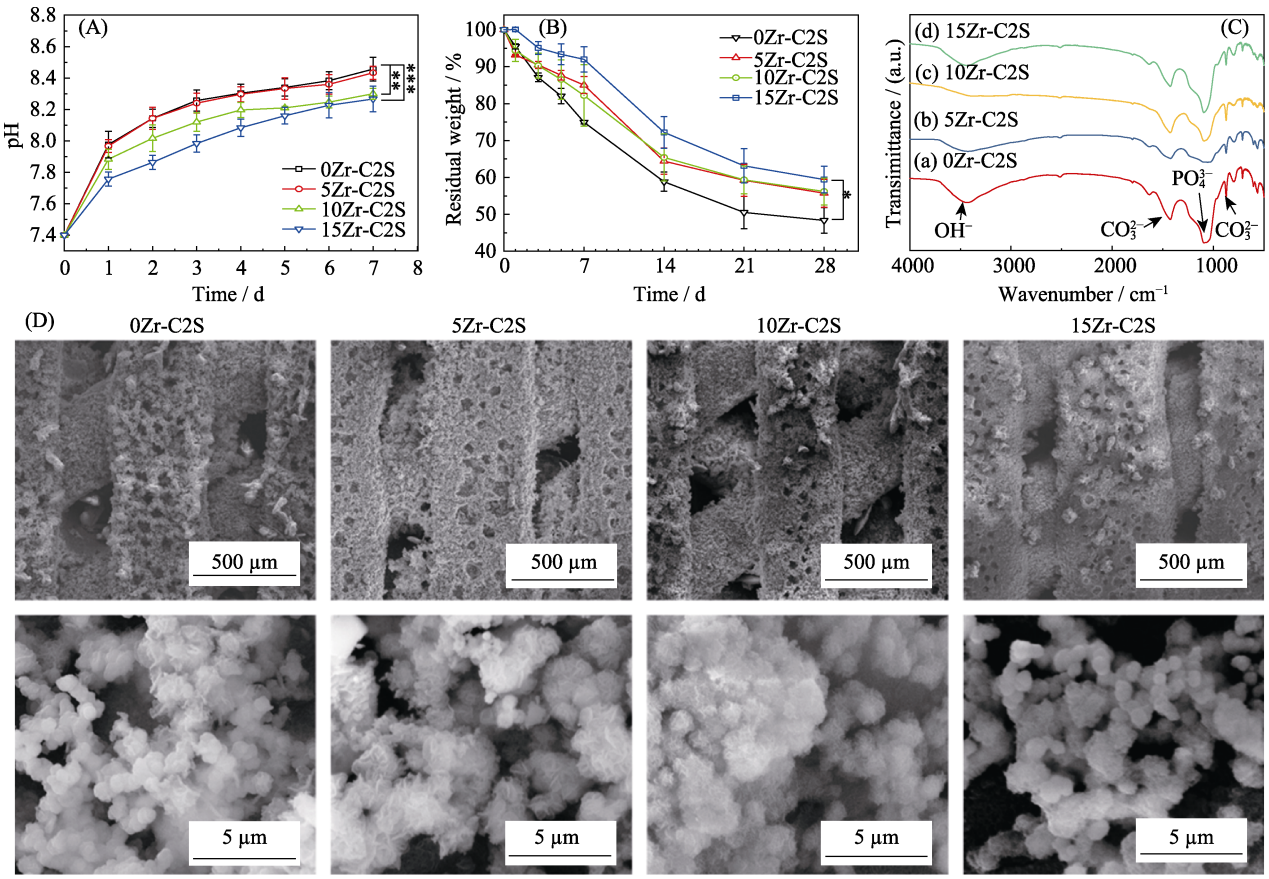

Fig. 4 (A) pH values and (B) *in vitro* degradation of the ZrO_2-incorporated β-Ca_2SiO_4 scaffolds in SBF (n = 3; *, ** and *** indicated significant differences, $P < 0.05$, $P < 0.01$ and $P < 0.001$), (C) FT-IR and (D) SEM images of the ZrO_2- incorporated scaffold surfaces after immersed in SBF for 7 d

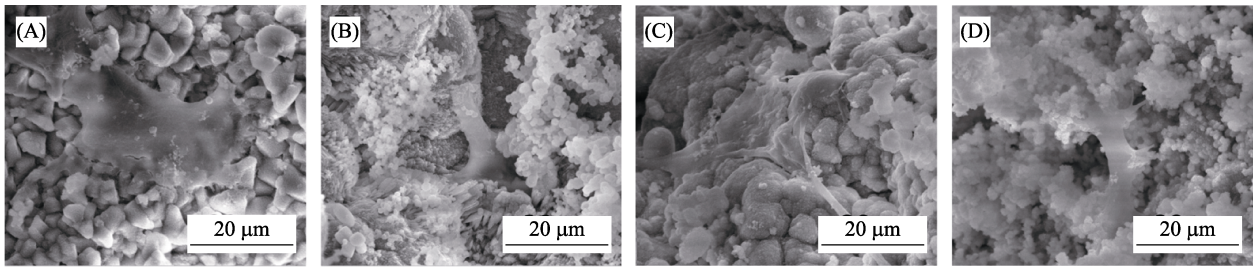

Fig. 5 SEM images of the attachment of rBMSCs on the ZrO_2-incorporated β-Ca_2SiO_4 scaffolds for 1 d, (A) 0Zr-C2S; (B) 5Zr-C2S; (C) 10Zr-C2S; (D) 15Zr-C2S

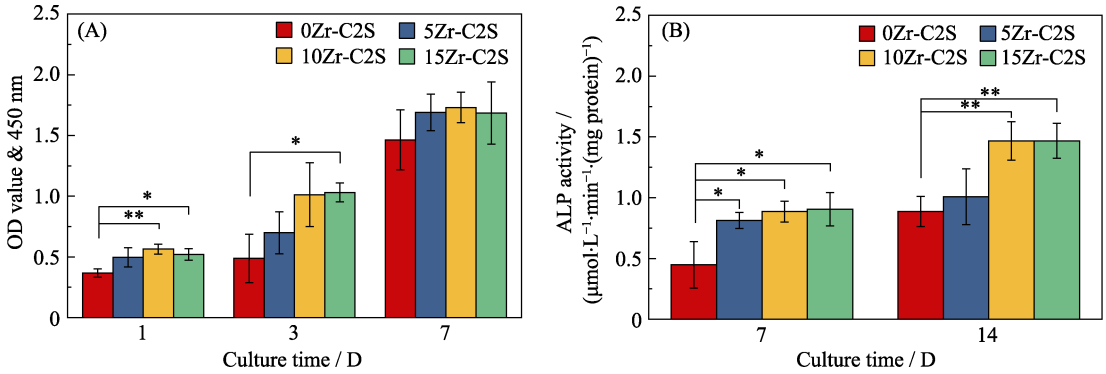

Fig. 6 (A) Quantitative analysis of the proliferation of rBMSCs cultured on β-Ca_2SiO_4 scaffolds for 3 and 7 d (n=3); (B) ALP activity of rBMSCs cultured for 7 and 14 d on β-Ca_2SiO_4 scaffolds for 7 and 14 d (n = 3, * and ** indicated significant differences, $P < 0.05$ and 0.01)

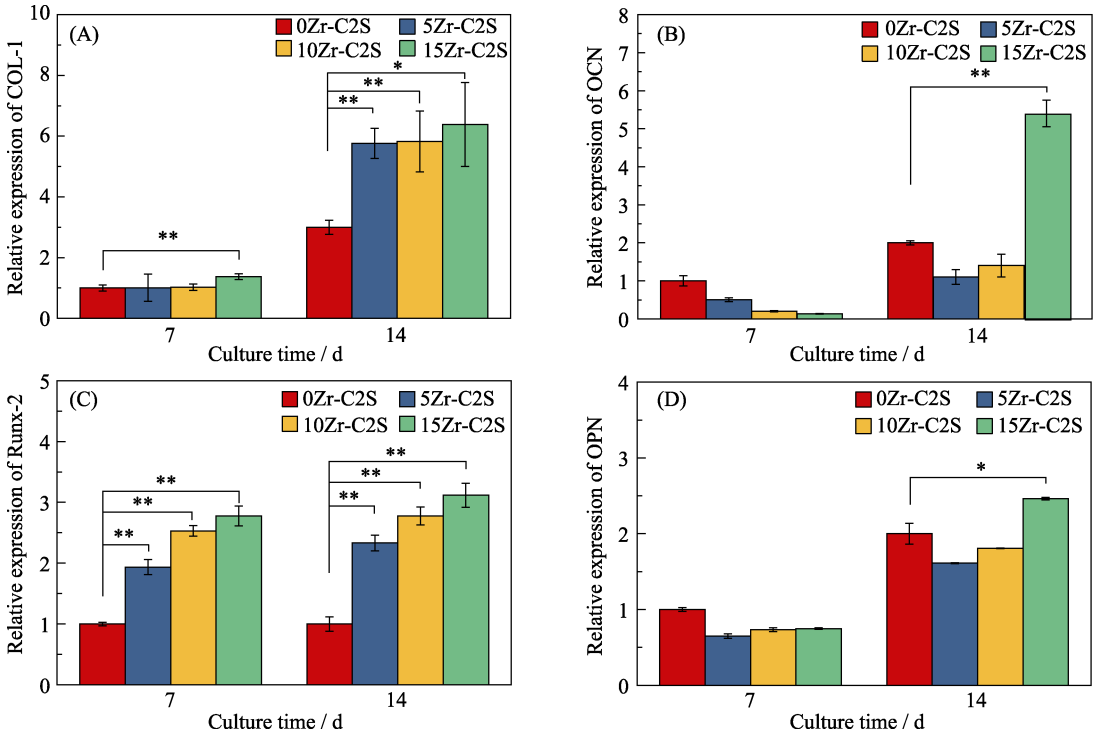

Fig. 7　Osteogenic expression of (A) COL-1, (B) OCN, (C) RunX-2 and (D) OPN for rBMSCs cultured on β-Ca2SiO4 scaffolds by qRT-PCR analysis after 7 and 14 d (n = 3; * and ** indicated significant differences, P < 0.05 and 0.01)

In detail, the new BMD of the 15Zr-C2S scaffolds ((0.6±0.03) g/cm^3) is significantly higher than that of the 0Zr-C2S scaffolds ((0.23±0.04) g/cm^3) and blank group (0.03 g/cm^3). Correspondingly, the 15Zr- C2S scaffolds showed the highest BV/TV ratio ((25±0.7)%) than the β-Ca_2SiO_4 scaffolds ((18.8±1.9)%) and blank group ((2.3±1.9)%). These results indicate that the ZrO_2-incorporated β-Ca_2SiO_4 scaffolds promote bone regeneration.

The new bone formation ability was also evaluated by the histological analysis. It can be clearly found that much more newly formed bone in the 15Zr-C2S scaffold group compared to pure β-Ca_2SiO_4 scaffold group and blank group (Fig. 9). The quantitative analysis of new bone area was determined by histomorphometric assay and they were 63.7±11.9, 33.6±3.5 and 23.6±1.5 for the 15Zr-C2S, 0Zr-C2S scaffolds and blank group, respectively.

3　Discussion

In this study, the ZrO_2-incorporated β-Ca_2SiO_4 scaffolds were successfully fabricated by polymer-derived technique and 3D printing. Silicone resin, $CaCO_3$ and ZrO_2 fillers are used as raw materials. The content of $CaCO_3$ active fillers and silicone resin fulfilled the stoichiometric ratio 2:1 of Ca/Si to obtain β-Ca_2SiO_4, and a part of $CaCO_3$ was substituted by ZrO_2 passive filler. To obtain a printable paste, the fillers were sieved and the paste was stirred to form homogeneous paste. A cylinder with regular and interconnected macropore structure was designed, which was maintained after sintering. The fabricated scaffolds with interconnected porous structure facilitate cell activities including attachment, migration, as well as flow transport of nutrients and bone ingrowth into scaffolds.

In the sintering process, silicone resin, as a reactant, first transferred into amorphous SiOC beyond 800 ℃[37], and then reacted with $CaCO_3$ active fillers to form β-Ca_2SiO_4[32], while ZrO_2 was passive and could not react with others during sintering. With the increase of sintering temperature, the diffusion capacity of the reactants improved, resulting in to a higher crystallinity of β-Ca_2SiO_4 (Fig. 1(B)). The crystallinity of the ZrO_2-incorporated β-Ca_2SiO_4 scaffolds was much lower (Fig. 1(A) and Fig. 2) due to the poor diffusion capacity of ZrO_2, which inhibited the crystallization of β-Ca_2SiO_4. On the other hand, all of scaffolds had rough surface on the struts with micropores, which is beneficial for cell adhesion as well. The volume shrinkage in the sintering process could be attributed to some small molecules evaporation and the polymer-to ceramic conversion, leading to the formation of micro-scale pores. At a higher temperature, β-Ca_2SiO_4 crystals formed and grew up, which partially filled the formed micro-pores. However, the incorporated ZrO_2 inhibited the crystallization of β-Ca_2SiO_4 during sintering, which also resulted in more micro-scale pores in the ZrO_2 incorporated β-Ca_2SiO_4 scaffolds than pure β-Ca_2SiO_4 scaffolds.

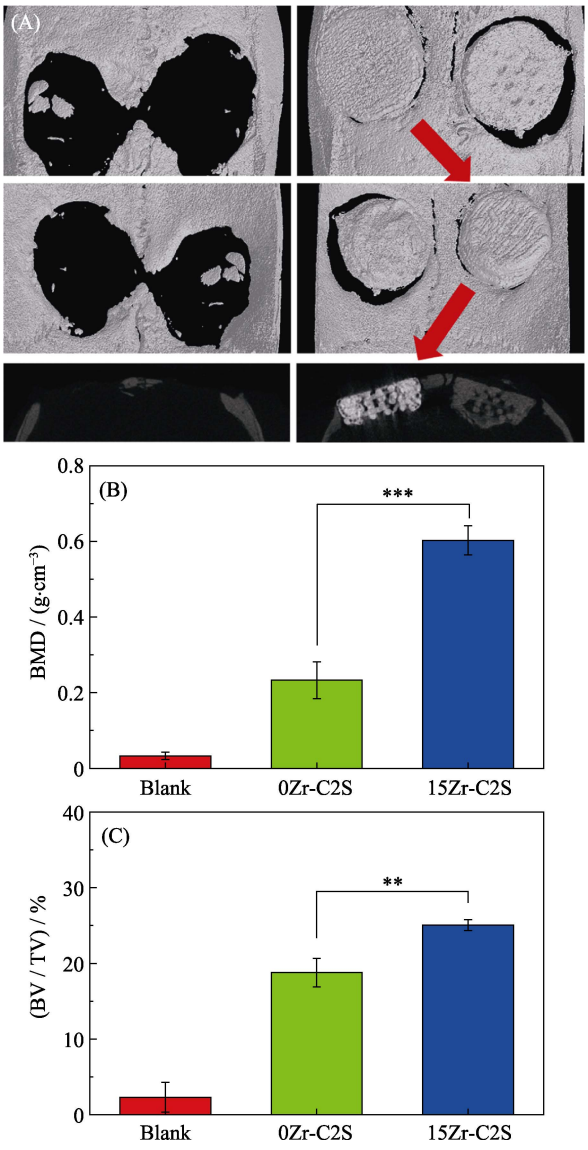

Fig. 8 Micro-CT evaluation of the repaired skulls at 8 weeks post-implantation

(A) 3D reconstruction and sagittal images showed the different reparative effects of blank group (left), 0Zr-C2S scaffolds (right, dark area), and 15Zr-C2S scaffolds (right, light area); (B) BMD and (C) BV/TV varied in every group (* p<0.05, ** p<0.01)

Mechanical strength is a vital factor for scaffolds because load-bearing is one of the important functions for bone implants. The compressive strength of the β-Ca_2SiO_4 scaffolds were remarkably enhanced by the ZrO_2 incorporation. As known, ZrO_2 has been commonly used in clinic due to its good biocompatibility and high toughness[17,36]. The ZrO_2 incorporation improved the compressive strength of the β-Ca_2SiO_4 scaffolds (Fig. 3). The increase of the mechanical strength is mainly because ZrO_2 is stronger than β-Ca_2SiO_4. On the other hand, high temperature induced the phase transition of ZrO_2 from monoclinic to tetragonal structure (> 1170 ℃)[35,38-39] (Fig. 1(B)). Tetragonal ZrO_2 is a metastable structure and easily changes into monoclinic structure induced by a

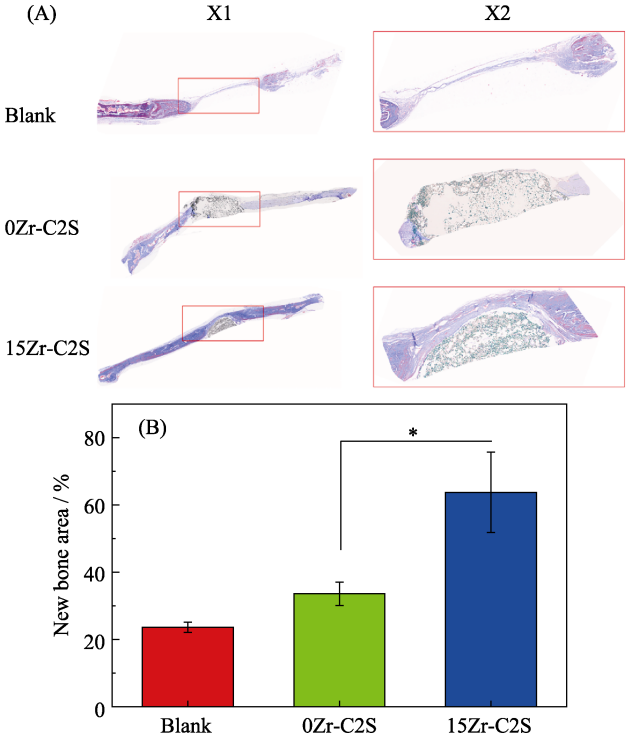

Fig. 9 (A) Histological analysis with (B) quantitative analysis of newly formed bone

Blue indicated new bone formation, and the scaffolds showed black (* p<0.05)

stress. In a stressed condition, the ZrO_2-incorporated scaffolds are able to transfer into stable monoclinic structure accompanied with a volume expansion, of which this phase transition is energy consumption and could absorb the external compressive energy. Thus, the ZrO_2-incorporation improved the mechanical strength of the scaffolds.

To explore the changes of the scaffolds in stimulated body fluid, pH and the residual weight of the scaffolds were measured. After soaking in SBF, the Ca ions released and reacted with H_3O ions, resulting in an alkali microenvironment and degradation of the scaffolds. However, the 15Zr-C2S scaffolds was favorable to achieve a more stable pH value with slower degradation, which could be attributed to the chemical stability of ZrO_2. The formation of apatite layer on the scaffold surface is also important for bonding to living bone tissue because the formation of an apatite layer means the ability of implant to form interfacial bonds with tissues when in contact with physiological fluid. After soaking in SBF for 7 d, the surface of each type of scaffolds were fully covered with spherical particle, and FT-IR verified the formation of like-apatite layer. Although ZrO_2 was inert in SBF, the apatite formation ability of the scaffolds was induced by β-Ca_2SiO_4. Followed by the reaction between Ca ions and H_3O ions, a rich-silicon layer forms and induces the formation of Ca–P nucleation with further formation of apatite crystal.

Previous studies demonstrated the good bioactivity for β-Ca_2SiO_4 scaffolds derived from silicone resin and $CaCO_3$ fillers. This study demonstrated that the ZrO_2-incorporated scaffolds were better for cell proliferation, differentiation and bone generation. rBMSCs were cultured on scaffolds and could easily attach on the surface of scaffolds (Fig. 5). The rough surfaces of scaffolds and the bioactive component contribute to the good cell attachment. Furthermore, β-Ca_2SiO_4 stimulated cell proliferation and differentiation to osteoblast. Interestingly, the scaffolds incorporated with more ZrO_2 showed enhanced levels of cell proliferation and osteogenic-related gene expression. As known, Ca ions plays an important role and their related signals affect the process of osteoblast differentiation[40-41]. For example, Ca increases the release of osteogenesis components such as insulin, glutamate by combing Ca-sensing receptors in cells. Maeno, *et al*[42] found that a certain range of Ca concentrations was suitable for osteoblast proliferation, differentiation and extracellular matrix mineralization, while exceeded calcium were cytotoxic. In this study, the degradation of the scaffolds led to Ca, Si ions release, and a faster degradation resulted to release more ions. Pure β-Ca_2SiO_4 possessed the fastest degradation and released highest amounts of Ca ions. By the substitution of ZrO_2 for Ca_2SiO_4 in the scaffolds, slower degradation was achieved, which maybe result in a more suitable amounts of Ca ions release, finally stimulated cell proliferation and differentiation to osteoblast. However, the concrete signal pathway to explain why exceeded Ca is harmful is unclear, which requires further study. On the other hand, exceeded Ca could induce a more alkali microenvironment, which was harmful to cell activity as well.

To investigate the scaffold's osteogenesis ability *in vivo*, the scaffolds were implanted into the critical-sized defects in rat model. The micro-CT quantitative analysis showed that the ZrO_2-incorporated β-Ca_2SiO_4 scaffolds significantly enhanced new bone formation. Histological analysis also showed that there was newly-formed bone in the β-Ca_2SiO_4 scaffolds, while the ZrO_2-incorporated scaffolds significantly promoted bone formation as well. Due to their apatite mineralization ability, cytocompatibility and the ability to induce cell differentiation into osteoblast, β-Ca_2SiO_4 scaffolds exhibited the ability for bone regeneration. The ZrO_2 incorporation could improve the compressive strength and the decreased Ca content in the scaffolds could adjust the pH microenvironment and degradation rate of the scaffolds, and cell activities. However, further investigations are required about the detailed functions of the ZrO_2-incorporated β-Ca_2SiO_4 scaffolds on facilitating new bone formation *in vivo*.

In summary, the ZrO_2 incorporation could increase the mechanical strength of the β-Ca_2SiO_4 scaffolds, and slow down the degradation rate of β-Ca_2SiO_4 scaffolds, which is beneficial for cell proliferation and differentiation to osteoblast, and final promote new bone formation.

4 Conclusion

β-Ca_2SiO_4 scaffolds incorporated with ZrO_2 were successfully derived from a silicone resin, $CaCO_3$ active fillers and ZrO_2 passive fillers by 3D printing. The fabricated scaffolds possessed interconnected macropore structure with high porosity (>67%) and compressive strength (ca. 6.1 MPa). The results indicated that the increase of ZrO_2 incorporation enhanced the compressive strength, and stimulated cell attachment, proliferation, differentiation to osteoblasts. Importantly, after implanting in rat defect sites, the ZrO_2-incorporated β-Ca_2SiO_4 scaffolds promoted new bone formation compared to the control group and the β-Ca_2SiO_4 scaffolds. Therefore, the 3D printed ZrO_2-incorporated β-Ca_2SiO_4 scaffolds would be a promising candidate for bone tissue engineering.

References:

[1] REZWAN K, CHEN Q Z, BLAKER J J, *et al.* Biodegradable and bioactive porous polymer/inorganic composite scaffolds for bone tissue engineering. *Biomaterials*, 2006, **27(18):** 3413–3431.

[2] GERHARDT LC, BOCCACCINI AR. Bioactive glass and glass-ceramic scaffolds for bone tissue engineering. *Materials (Basel)*, 2010, **3(7):** 3867–38910.

[3] ZHU Y, LI X, YANG J, *et al.* Composition–structure–property relationships of the $CaO–M_xO_y–SiO_2–P_2O_5$ (M=Zr, Mg, Sr) mesoporous bioactive glass (MBG) scaffolds. *Journal of Materials Chemistry*, 2011, **21(25):** 9208–9218.

[4] XIN C, QI X, ZHU M, *et al.* Hydroxyapatite whisker-reinforced composite scaffolds through 3D printing for bone repair. *Journal of Inorganic Materials*, 2017, **32(8):** 837–844.

[5] ZHU M, HUANG T, DU X, *et al.* Progress of the 3D printing technology for biomaterials. *Journal of University of Shanghai for Science and Technology*, 2017, **39(5):** 473–489.

[6] DAI Y, LIU H, LIU B, *et al.* Porous β-Ca_2SiO_4 ceramic scaffolds for bone tissue engineering: *in vitro* and *in vivo* characterization. *Ceramics International*, 2015, **41(4):** 5894–5902.

[7] GOU Z, CHANG J, ZHAI W, *et al.* Study on the self-setting property and the *in vitro* bioactivity of beta-Ca_2SiO_4. *Journal of Biomedical Materials Research Part B-Applied Biomaterials*, 2005, **73(2):** 244–251.

[8] GOU Z, CHANG J. Synthesis and *in vitro* bioactivity of dicalcium silicate powders. *Journal of the European Ceramic Society*, 2004, **24(1):** 93–99.

[9] GOU Z, CHANG J, ZHAI W. Preparation and characterization of novel bioactive dicalcium silicate ceramics. *Journal of the European Ceramic Society*, 2005, **25(9):** 1507–1514.

[10] PEI P, WEI D, ZHU M, *et al.* The effect of calcium sulfate incorporation on physiochemical and biological properties of 3D-printed mesoporous calcium silicate cement scaffolds. *Microporous and Mesoporous Materials*, 2017, **241:** 11–20.

[11] BAINO F, VITALE-BROVARONE C. Bioceramics in ophthalmology. *Acta Biomaterialia*, 2014, **10(8):** 3372–3397.

[12] FU Q, SAIZ E, RAHAMAN MN, *et al.* Bioactive glass scaffolds for bone tissue engineering: state of the art and future perspectives. *Materials Science & Engineering C-Materials for Biological Applications*, 2011, **31(7):** 1245–1256.

[13] CHOUDHARY R, VENKATRAMAN SK, RANA A, *et al. In vitro* bioactivity studies of larnite and larnite/chitin composites prepared from biowaste for biomedical applications. *Bulletin of Materials Science*, 2016, **39(5):** 1213–1221.

[14] PEI P, QI X, DU X, *et al.* Three-dimensional printing of tricalcium silicate/mesoporous bioactive glass cement scaffolds for bone re-

generation. *Journal of Materials Chemistry B*, 2016, **4(46):** 7452–7463.
[15] ZHANG J, ZHAO S, ZHU M, *et al.* 3D-printed magnetic Fe_3O_4/MBG/PCL composite scaffolds with multifunctionality of bone regeneration, local anticancer drug delivery and hyperthermia. *Journal of Materials Chemistry B*, 2014, **2(43):** 7583–7595.
[16] ZHANG J, ZHAO S, ZHU Y, *et al.* Three-dimensional printing of strontium-containing mesoporous bioactive glass scaffolds for bone regeneration. *Acta Biomaterialia*, 2014, **10(5):** 22692281.
[17] DU X, FU S, ZHU Y. 3D printing of ceramic-based scaffolds for bone tissue engineering: an overview. *Journal of Materials Chemistry B*, 2018, **6(27):** 4397–4412.
[18] DU X, YU B, PEI P, *et al.* 3D printing of pearl/$CaSO_4$ composite scaffolds for bone regeneration. *Journal of Materials Chemistry B*, 2018, **6(3):** 499–509.
[19] ZHU M, LI K, ZHU Y, *et al.* 3D-printed hierarchical scaffold for localized isoniazid/rifampin drug delivery and osteoarticular tuberculosis therapy. *Acta Biomaterialia*, 2015, **16:** 145–455.
[20] QI X, PEI P, ZHU M, *et al.* Three dimensional printing of calcium sulfate and mesoporous bioactive glass scaffolds for improving bone regeneration *in vitro* and *in vivo*. *Sciencitic Reports*, 2017, **7:** 42556–1–12.
[21] ZHAO S, ZHANG J, ZHU M, *et al.* Three-dimensional printed strontium-containing mesoporous bioactive glass scaffolds for repairing rat critical-sized calvarial defects. *Acta Biomaterialia*, 2015, **12:** 270–280.
[22] ZHU M, ZHAO SC, XIN C, *et al.* 3D-printed dimethyloxallyl glycine delivery scaffolds to improve angiogenesis and osteogenesis. *Biomateral Science*, 2015, **3(8):** 1236–1244.
[23] PEI P, TIAN Z F, ZHU Y F. 3D printed mesoporous bioactive glass/metal-organic framework scaffolds with antitubercular drug delivery. *Microporous and Mesoporous Materials*, 2018, **272:** 24–30.
[24] PIRES I, GOUVEIA B, RODRIGUES J, *et al.* Characterization of sintered hydroxyapatite samples produced by 3D printing. *Rapid Prototyping Journal*, 2014, **20(5):** 413–421.
[25] XIE J, SHAO H, HE D, *et al.* Ultrahigh strength of three-dimensional printed diluted magnesium doping wollastonite porous scaffolds. *MRS Communications*, 2015, **5(4):** 631–639.
[26] BERNARDO E, COLOMBO P, DAINESE E, *et al.* Novel 3D Wollastonite-based scaffolds from preceramic polymers containing micro- and nano-sized reactive particles. *Advanced Engineering Materials*, 2012, **14(4):** 269–274.
[27] ELSAYED H, COLOMBO P, BERNARDO E. Direct ink writing of wollastonite-diopside glass-ceramic scaffolds from a silicone resin and engineered fillers. *Journal of the European Ceramic Society*, 2017, **37(13):** 4187–4195.
[28] ZOCCA A, ELSAYED H, BERNARDO E, *et al.* 3D-printed silicate porous bioceramics using a non-sacrificial preceramic polymer binder. *Biofabrication*, 2015, **7(2):** 025008–1–12.
[29] ELSAYED H, SINICO M, SECCO M, *et al.* B-doped hardystonite bioceramics from preceramic polymers and fillers: synthesis and application to foams and 3D-printed scaffolds. *Journal of the European Ceramic Society*, 2017, **37(4):** 1757–1767.
[30] ZOCCA A, FRANCHIN G, ELSAYED H, *et al.* Direct ink writing of a preceramic polymer and fillers to produce hardystonite ($Ca_2ZnSi_2O_7$) bioceramic scaffolds. *Journal of the American Ceramic Society*, 2016, **99(6):** 1960–1967.
[31] FIOCCO L, ELSAYED H, BADOCCO D, *et al.* Direct ink writing of silica-bonded calcite scaffolds from preceramic polymers and fillers. *Biofabrication*, 2017, **9(2):** 025012–1–13.
[32] FU S, LIU W, LIU S, *et al.* 3D printed porous β-Ca_2SiO_4 scaffolds derived from preceramic resin and their physicochemical and biological properties. *Science and Technology of Advanced Materials*, 2018, **19(1):** 495–506.
[33] WU C, RAMASWAMY Y, SOEPARTO A, *et al.* Incorporation of titanium into calcium silicate improved their chemical stability and biological properties. *Journal of Biomedical Materials Research Part A*, 2008, **86(2):** 402–410.
[34] KO H C, HAN J S, BACHLE M, *et al.* Initial osteoblast-like cell response to pure titanium and zirconia/alumina ceramics. *Dental Materials*, 2007, **23(11):** 1349–1355.
[35] HANNINK R H J, KELLY P M, MUDDLE B C. Transformation toughening in zirconia-containing ceramics. *Journal of the American Ceramic Society*, 2000, **83(3):** 461–487.
[36] CHEVALIER J. What future for zirconia as a biomaterial? *Biomaterials*, 2006, **27(4):** 535–543.
[37] ECKEL ZC, ZHOU C, MARTIN JH, *et al.* Additive manufacturing of polymer-derived ceramics. *Science*, 2016, **351(6268):** 58–62.
[38] IONESCU E, LINCK C, FASEL C, *et al.* Polymer-derived SiOC/ZrO_2 ceramic nanocomposites with excellent high-temperature stability. *Journal of the American Ceramic Society*, 2010, **93(1):** 241–250.
[39] CHEVALIER J, GREMILLARD L, VIRKAR A V, *et al.* The tetragonal-monoclinic transformation in zirconia: lessons learned and future trends. *Journal of the American Ceramic Society*, 2009, **92(9):** 1901–1920.
[40] HOPPE A, GULDAL N S, BOCCACCINI A R. A review of the biological response to ionic dissolution products from bioactive glasses and glass-ceramics. *Biomaterials*, 2011, **32(11):** 2757–2774.
[41] MAJIDINIA M, SADEGHPOUR A, YOUSEFI B. The roles of signaling pathways in bone repair and regeneration. *Journal of Cellular Physiology*, 2018, **233(4):** 2937–2948.
[42] MAENO S, NIKI Y, MATSUMOTO H, *et al.* The effect of calcium ion concentration on osteoblast viability, proliferation and differentiation in monolayer and 3D culture. *Biomaterials*, 2005, **26(23):** 4847–4855.

二氧化锆掺入对三维打印的硅酸二钙支架物理化学和生物学性能的影响

傅声扬[1], 俞 斌[2], 丁惠锋[2,3], 石国栋[2], 朱钰方[1]

(1. 上海理工大学 材料科学与工程学院, 上海 200093; 2. 复旦大学 上海医学院, 上海市公共卫生临床中心 骨科, 上海 200032; 3. 上海市浦东医院复旦大学附属浦东医院 201399)

摘 要: 三维打印结合高分子前躯体制备生物陶瓷材料由于制备工艺简单, 在骨组织工程修复领域引起了极大的关注。本文成功利用三维打印技术与高分子硅胶前躯体结合, 通过填充活性 $CaCO_3$ 和惰性 ZrO_2 制备出 ZrO_2 掺杂的 β-Ca_2SiO_4 支架。制备得到的支架具有均一、连通的大孔结构(孔隙率>67%), 随着掺杂 ZrO_2 含量的增加, 支架的抗压强度明显提高, 并且促进成骨细胞增殖、分化。重要的是在动物体内实验发现, 相较于纯的 β-Ca_2SiO_4 支架, ZrO_2 的掺入明显提高了支架在骨缺损处促进新骨形成的能力。因而, 通过三维打印结合高分子前躯体技术制备掺杂 ZrO_2 的 β-Ca_2SiO_4 支架有望应用于骨组织工程。

关 键 词: β-Ca_2SiO_4; ZrO_2; 聚合物前驱; 三维打印; 骨组织工程

中图分类号: TQ174 **文献标识码:** A